LETTER

A resonant chain of four transiting, sub–Neptune planets

Sean M. Mills[1], Daniel C. Fabrycky[1], Cezary Migaszewski[2,3], Eric B. Ford[4,5,6], Erik Petigura[7,8] & Howard Isaacson[7]

Surveys have revealed many multi-planet systems containing super-Earths and Neptunes in orbits of a few days to a few months[1]. There is debate whether *in situ* assembly[2] or inward migration is the dominant mechanism of the formation of such planetary systems. Simulations suggest that migration creates tightly packed systems with planets whose orbital periods may be expressed as ratios of small integers (resonances)[3–5], often in a many-planet series (chain)[6]. In the hundreds of multi-planet systems of sub-Neptunes, more planet pairs are observed near resonances than would generally be expected[7], but no individual system has hitherto been identified that must have been formed by migration. Proximity to resonance enables the detection of planets perturbing each other[8]. Here we report transit timing variations of the four planets in the Kepler-223 system, model these variations as resonant-angle librations, and compute the long-term stability of the resonant chain. The architecture of Kepler-223 is too finely tuned to have been formed by scattering, and our numerical simulations demonstrate that its properties are natural outcomes of the migration hypothesis. Similar systems could be destabilized by any of several mechanisms[5,9–11], contributing to the observed orbital-period distribution, where many planets are not in resonances. Planetesimal interactions in particular are thought to be responsible for establishing the current orbits of the four giant planets in the Solar System by disrupting a theoretical initial resonant chain[12] similar to that observed in Kepler-223.

Kepler-223 is a known four-planet system[13] orbiting around a slightly evolved (about 6-Gyr-old), Sun-like star (see Methods, Extended Data Fig. 1). The low observational signal-to-noise ratio initially caused an incorrect identification of the orbital periods of this system[13,14], and has hitherto precluded its detailed characterization. For the analysis of transit timing variation (TTV), we use long cadence (29.4-min

integrations) data, collected over the full duration of NASA's Kepler Space Mission from March 2009 to May 2013. Over this window, the ratios of the orbital periods (P) of planets b, c, d and e (named in alphabetic order from the interior, beginning with b) average $P_c/P_b = 1.3336$, $P_d/P_c = 1.5015$ and $P_e/P_d = 1.3339$ (ref. 15). We expect a system with periods so close to resonance to exhibit TTVs due to planet–planet interactions[8] (see Methods).

To measure TTVs, we bin the data into 3-month segments based on Kepler's observing quarters, confirm that the orbital periods are near resonances, and demonstrate the time-variable nature of the transits (Fig. 1, Extended Data Fig. 2, Extended Data Table 1 and Methods). Phase folding the data and removing the TTVs allows the noisy transits to be identified easily by eye (Fig. 2).

The behaviour of the resonant chain can be characterized by its Laplace angles: $\phi_1 \equiv -\lambda_b + 2\lambda_c - \lambda_d$, $\phi_2 \equiv \lambda_c - 3\lambda_d + 2\lambda_e$ (for mean longitudes λ_i and planets $i = $ b, c, d, e) and, for the whole system of four planets, $\phi_3 \equiv 2\phi_2 - 3\phi_1 = 3\lambda_b - 4\lambda_c - 3\lambda_d + 4\lambda_e$. Systems that are in resonance possess such librating Laplace angles, which ensures that two planets have a close approach when the other planets are far away, reducing chaotic interactions. The existence of a single four-body Laplace angle demonstrates that all the planets have close dynamical contact (with various three- and two-body resonances also present). We infer variations in the Laplace angles directly from the measured TTVs (see Methods and Extended Data Fig. 3). If we assume nearly circular orbits, the four years of TTVs in the data have recorded both angles performing nearly a full oscillation; ϕ_1 librates between approximately 173° and 190° and ϕ_2 librates between approximately 47° and 75°.

To improve the treatment of the TTV signal and directly connect it to planetary dynamics, we integrate the N-body equations of motion for the four-planet system and explicitly model the photometric transit signals over the Kepler observing window (photodynamical modelling)[16].

Table 1 | Kepler-223 system parameters

Parameter name	DEMCMC result			
Spectroscopic stellar mass, $M_\star$ ($M_\odot$)	$1.125^{+0.094}_{-0.073}$			
Stellar radius, $R_\star$ ($R_\odot$)	$1.72^{+0.07}_{-0.14}$			
	Kepler-223 b	Kepler-223 c	Kepler-223 d	Kepler-223 e
Orbital period, P (d)	$7.38449^{+0.00022}_{-0.00022}$	$9.84564^{+0.00052}_{-0.00051}$	$14.78869^{+0.00030}_{-0.00027}$	$19.72567^{+0.00055}_{-0.00054}$
Eccentricity, e	$0.078^{+0.015}_{-0.017}$	$0.150^{+0.019}_{-0.051}$	$0.037^{+0.018}_{-0.017}$	$0.051^{+0.019}_{-0.019}$
Inclination, $|i-90|$ (°)	$0.0^{+1.8}$	$0.0^{+1.3}$	$2.06^{+0.26}_{-0.32}$	$2.00^{+0.21}_{-0.27}$
Mass, M ($M_\oplus$)	$7.4^{+1.3}_{-1.1}$	$5.1^{+1.7}_{-1.1}$	$8.0^{+1.5}_{-1.3}$	$4.8^{+1.4}_{-1.2}$
Radius, R ($R_\oplus$)	$2.99^{+0.18}_{-0.27}$	$3.44^{+0.20}_{-0.30}$	$5.24^{+0.26}_{-0.45}$	$4.60^{+0.27}_{-0.41}$
Density, ρ (g cm^{-3})	$1.54^{+0.63}_{-0.35}$	$0.71^{+0.33}_{-0.20}$	$0.31^{+0.12}_{-0.07}$	$0.28^{+0.12}_{-0.08}$

Medians and 68% credible intervals for planet properties based on 2,008 10^6-year stable solutions with eccentricity priors as described in Methods: $(e_{b,max}, e_{c,max}, e_{d,max}, e_{e,max}) = (0.212, 0.175, 0.212, 0.175)$ and fixed nodal angle $\Omega_j = 0$ for $j = $ b, c, d, e. All values are valid at an epoch time $T_{epoch} = 800.0$ (BJD $-$ 2,454,900). The stellar mass ($M_\star$) was held fixed in the differential-evolution Markov chain Monte Carlo (DEMCMC) simulation, but uncertainties in planetary mass were adjusted afterward to account for the quoted spectroscopic uncertainty in $M_\star$. $M_\odot$ and $R_\odot$ are the mass and radius of the Sun, respectively; $M_\oplus$ and $R_\oplus$ are the mass and radius of Earth. See Methods and Extended Data Table 2 for additional parameters and discussion.

[1]Department of Astronomy and Astrophysics, The University of Chicago, 5640 South Ellis Avenue, Chicago, Illinois 60637, USA. [2]Institute of Physics and CASA*, University of Szczecin, Wielkopolska 15, 70-451 Szczecin, Poland. [3]Torun Centre for Astronomy, Nicolaus Copernicus University, Gagarina 11, 87-100 Torun, Poland. [4]Center for Exoplanets and Habitable Worlds, The Pennsylvania State University, University Park, Pennsylvania 16802, USA. [5]Department of Astronomy and Astrophysics, The Pennsylvania State University, University Park, Pennsylvania 16802, USA. [6]Center for Astrostatistics, The Pennsylvania State University, University Park, Pennsylvania 16802, USA. [7]University of California at Berkeley, Berkeley, California 94720, USA. [8]California Institute of Technology, Pasadena, California 91125, USA.
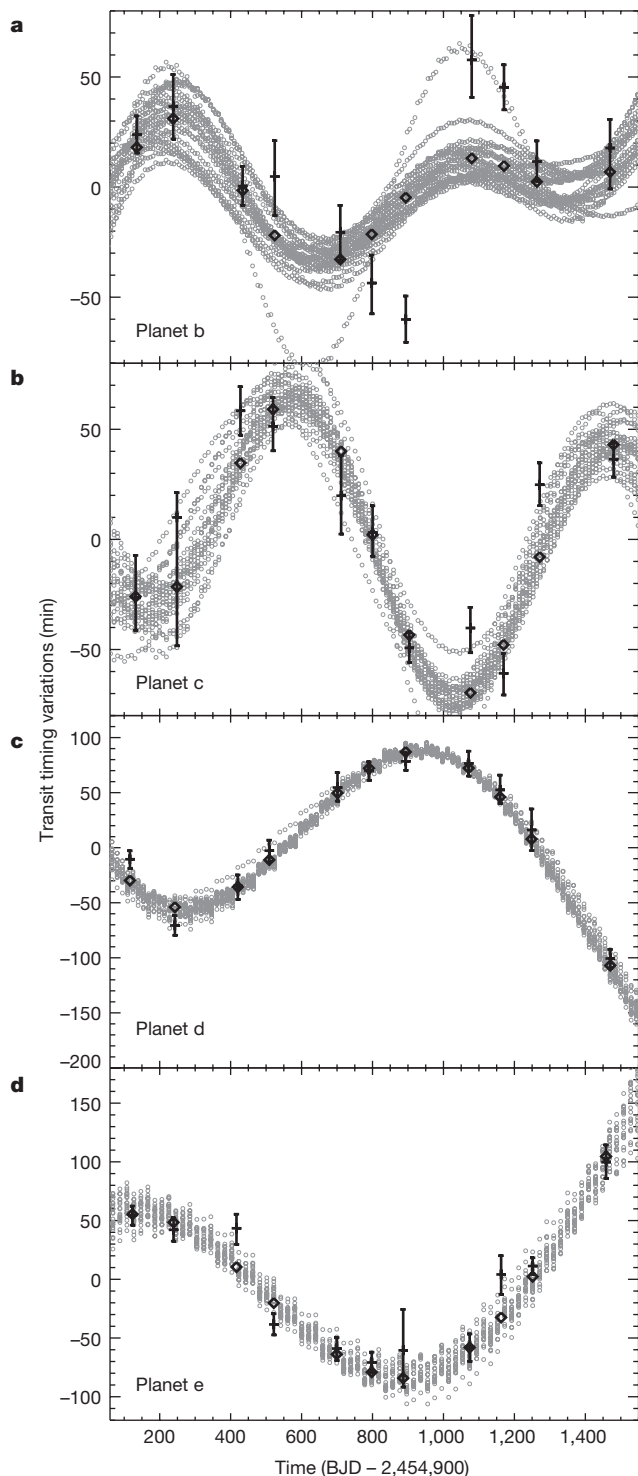
Figure 1 | Transit timing variations (TTVs) for all four planets with respect to a linear ephemeris. a–d, Calculated transit times for planets b–e, respectively, come from a linear regression of the best-fit model transits. Open grey circles show the transit times from 20 different models that were stable over a 10^7-year simulation. Black '+' symbols with 1σ error bars indicate the TTVs found by fitting quarterly binned data (see Extended Data Fig. 2), and black diamonds are the corresponding points for the mean of the grey-circle models binned in the same manner. Where the noise causes large uncertainties, the photodynamic model may deviate from the binned data, but more accurately reflects the true TTVs. BJD, barycentric Julian date.

We determine best estimates and uncertainties for the system parameters by performing five-body integrations of initial conditions from the resulting posterior distribution for more than 10^7 orbits of the planets
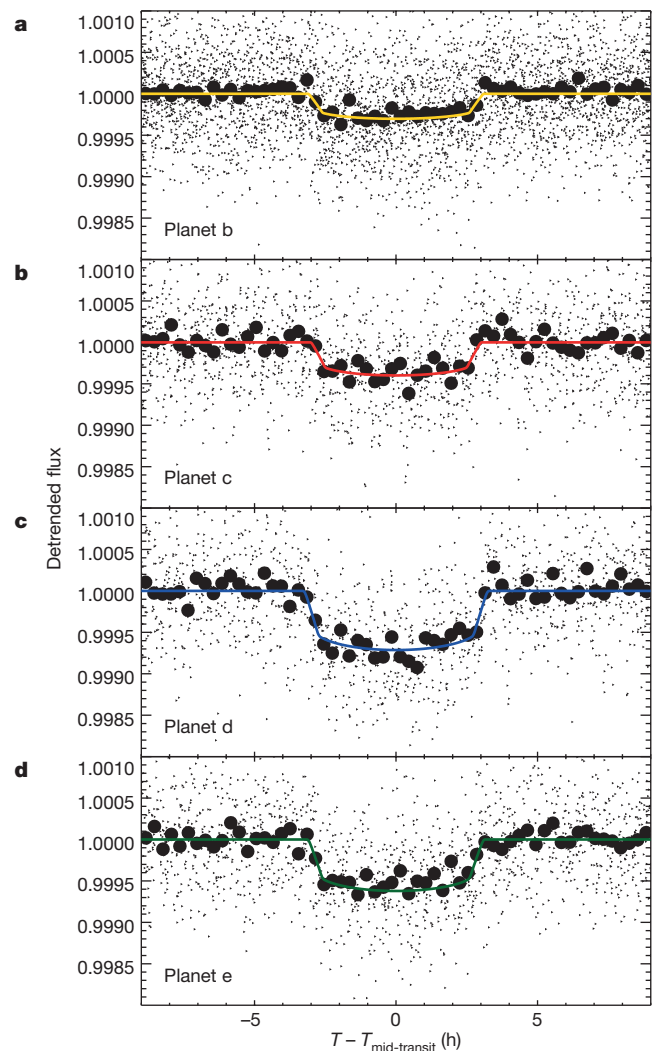

Figure 2 | Binned planet transits. a–d, Photometry data near transits of planets b–e, respectively (small black triangles), binned together (large black circles) by phase-folding after removing the measured TTV for each quarter. Systematic trends have been removed and the flux normalized to 1.0 out of transit. The coloured lines are the best-fit transit models to the data.

and retaining only parameter sets that remain stable (see Methods for details). We find that the planets all have masses of $3M_\oplus$–$9M_\oplus$ and radii of $2.5R_\oplus$–$5.5R_\oplus$ ($M_\oplus$ and $R_\oplus$ are the mass and radius of Earth, respectively; see Table 1). On the basis of these values and internal structure models[17], we determine that the composition of the planets varies from about 1% to 5% H/He by mass for the innermost planet to more than about 10% by mass for the outermost planet; that is, they are all sub-Neptunes. The density of the planets decreases with orbital semi-major axis, consistent with scenarios involving atmospheric loss due to stellar irradiation or formation in regions of increasingly cooler temperatures[18]. The eccentricities of the planets are relatively low (about $0.01-0.1$) in configurations that are stable for more than 10^7 orbits of the system. To fit the data acceptably, the eccentricities need to be slightly larger than in other systems of sub-Neptunes such as Kepler-11, whose eccentricities are less than about 0.02 (ref. 19). Because the eccentricities may be excited and stabilized by the resonances, the system can remain stable even though it is compact. The eccentricity of a planet is only loosely negatively correlated with its mass (from the TTVs in the data), so small changes in the allowed eccentricity will have a small effect on the posterior mass estimate, and removing eccentricity constraints would make the planets only slightly less dense.

Periods in a ratio close to 3:4:6:8 are maintained in all the stable, data-fitting solutions. The range of the ratios of the osculating periods
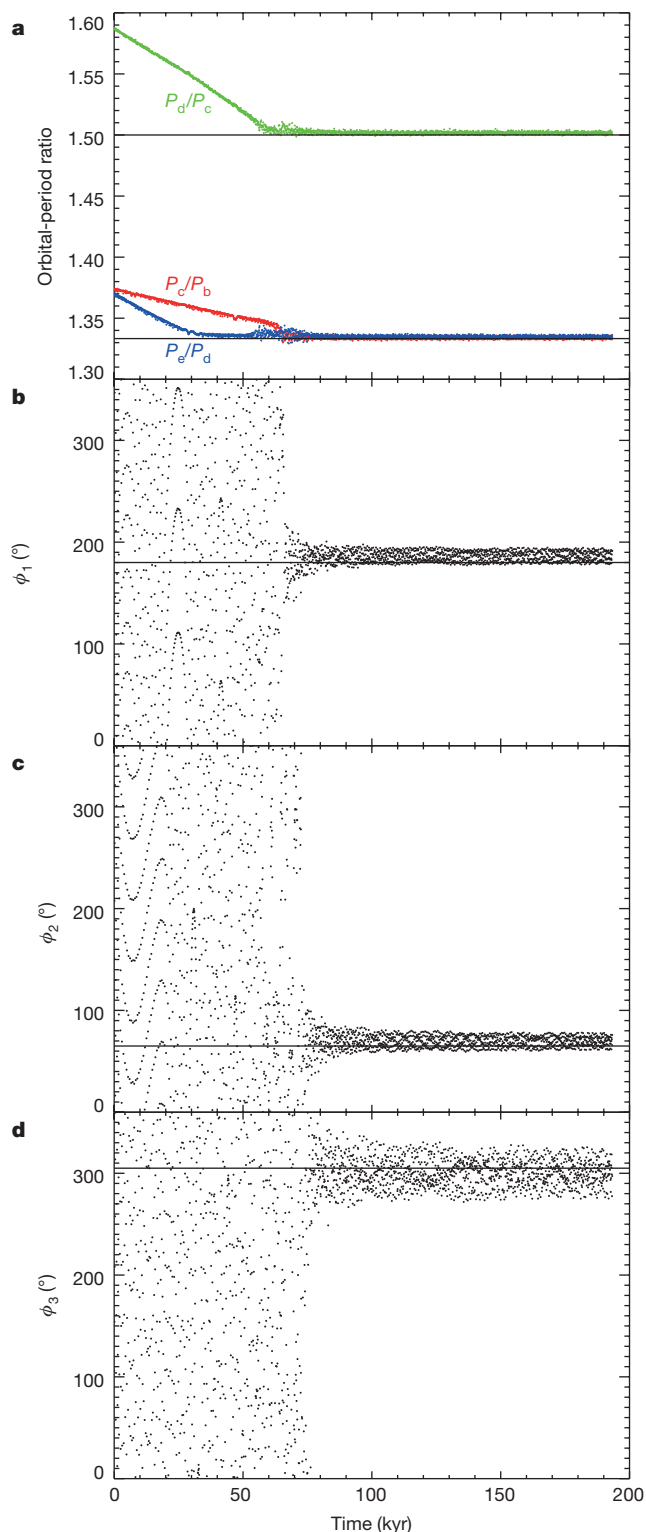
Figure 3 | A migration simulation that ends in a configuration matching the observed semi-major axis ratios, and libration angle centres and amplitudes. a, Time evolution of orbital-period ratios of planets b and c (P_c/P_b; red), c and d (P_d/P_c; green), and d and e (P_e/P_d; blue) in a migration simulation. **b–d**, Time evolution of the Laplace angles (ϕ_{1-3}) defined in the text. The resonant angles and libration amplitudes that the planets end up in (indicated by the black horizontal lines) match those observed in the data (see, for example, Extended Data Fig. 3).

of the planets implied by the observed TTVs over the Kepler window is typical for a resonant system. This range is narrower than that for a long-lived (more than about 10^7 orbits), but circulating

(non-resonant), solution (Extended Data Figs 4, 5), suggesting that the system is currently in a state of libration. This libration might be temporary, and periods of Laplace-angle circulation might have occurred previously or might occur in the future for this system. However, requiring short-term Laplace-angle libration substantially increases the likelihood that a parameter set that acceptably fits the data represents a long-lived system (see Methods). Because (i) the orbital parameters of Kepler-223 are consistent with it being in a resonant state, (ii) solutions that are stable for 100 Myr exist within the parameter posteriors, and (iii) resonance greatly helps a system this compact to remain stable, we conclude that the system is probably a true resonant chain.

Planetary migration in a disk has been extensively studied and often leads to resonant chains of planets[3–6]. To examine the plausibility of the specific resonant chain observed in Kepler-223, we use a previously developed model[20] to simulate the migration of four planets within a gas disk. We find that four planets starting well wide of resonance migrate inwards and converge to the 3:4:6:8 chain of periods that we observe with certain choices of simulation parameters (Fig. 3). Thus the Kepler-223 system is a plausible outcome of disk migration, but the full set of disk migration parameters and initial conditions that would lead to this system remains an open question.

In a migration scenario, systems trapped in resonances for which the orbital semi-major axes are small (less than about 0.5 AU) can potentially be used to constrain the rate of disk photoevaporation and the lifetimes of disks, because a gaseous disk must exist in the 0.02–0.2 AU range long enough for planets of moderate mass to migrate. It also provides constraints on turbulence and magnetic fields in the disk[21], and the structure of the disk that causes the planets to stop migrating[22]. An alternative to gas-disk migration for trapping planets into resonances is migration via planetesimal scattering[23]. It is possible for planetesimal scattering to migrate two planets in a convergent manner, establishing a resonance. However, this convergent migration would excite the eccentricities of the planetesimal population, which would probably prevent additional planets from joining the resonance[24]. The presence of a large volatile (greater than about 10% H/He by mass)[17] layer on the outer planets also suggests that the planets formed in the presence of a gas-containing disk at cool temperatures, further suggesting large-scale migration[18].

Several other exoplanet systems have (GJ 876; ref. 25), or are speculated to have (HR 8799; ref. 20), resonant chains, but these are composed of planets that are substantially more massive and have much greater orbital distances; hence, these observations may not be relevant to the formation of systems of close-in sub-Neptunes. Several Kepler systems are probably in a true resonance (as opposed to near resonance; for example, the 6:5 system Kepler-50 and the 5:4:3 system Kepler-60; ref. 26); however, owing to the large number of known multi-planet systems, even if the orbital-period ratios of planets are essentially random, consistent with *in situ*, giant-impact formation, we would expect to observe some systems whose period ratios were near enough to integer values that they entered true dynamical resonances. By contrast, the precise conditions for the four-planet resonant chain of Kepler-223 cannot be accounted for by random selection of period ratios[7], and the system is probably too fragile to have been assembled by giant impacts[27].

The dynamical fragility of Kepler-223 suggests that resonant chains were precursors to some of the more common, non-resonant systems and that planet–planet scattering post-formation is probably an important step in creating the observed period distribution[10]. A model of the formation of the Solar System that has parallels with observed exoplanets involves the four giant planets entering a series of resonances, reaching their current configuration only after destabilization hundreds of millions of years later[12]. Numerical simulations for Kepler-223 indicate that only a small mass of orbit-crossing planetesimals is needed to move Kepler-223 off resonance[28], but that it could escape this fate if intrinsic differences in protoplanetary disks resulted in the lack of such a planetesimal population. In fact, various mechanisms including disk

dissipation[9], planet–planet scattering[10], tidal dissipation[5] and planetesimal scattering[11] could break migration-induced resonances in the majority of exoplanet systems. It has been suggested that some multi-resonant systems (for example, Kepler-80, which has planetary pairs near, but not in, two-body resonances) might have undergone resonant disruption as a result of tidal dissipation, which would explain most of the period ratios that are slightly greater than resonant values in Kepler data[29,30]. It is possible that the Kepler-223 resonance has survived as a result of its relatively more distant innermost planet. Overall, we suggest that substantial migration of planets, including epochs of resonance that are typically only temporary, rather than *in situ* formation, leads to the final, observed planetary orbits for many close-in sub-Neptune systems.

Online Content Methods, along with any additional Extended Data display items and Source Data, are available in the online version of the paper; references unique to these sections appear only in the online paper.

1. Mullally, F. *et al.* Planetary candidates observed by *Kepler*. VI. Planet sample from Q1–Q16 (47 months). *Astrophys. J. Suppl. Ser.* **217,** 31 (2015).
2. Hansen, B. M. S. & Murray, N. Testing in situ assembly with the *Kepler* planet candidate sample. *Astrophys. J.* **775,** 53 (2013).
3. Melita, M. D. & Woolfson, M. M. Planetary commensurabilities driven by accretion and dynamical friction. *Mon. Not. R. Astron. Soc.* **280,** 854–862 (1996).
4. Lee, M. H. & Peale, S. J. Dynamics and oigin of the 2:1 orbital resonances of the GJ 876 planets. *Astrophys. J.* **567,** 596–609 (2002).
5. Terquem, C. & Papaloizou, J. C. B. Migration and the formation of systems of hot super-Earths and Neptunes. *Astrophys. J.* **654,** 1110–1120 (2007).
6. Cresswell, P. & Nelson, R. P. On the evolution of multiple protoplanets embedded in a protostellar disc. *Astron. Astrophys.* **450,** 833–853 (2006).
7. Fabrycky, D. C. *et al.* Architecture of *Kepler*'s multi-transiting systems. II. New investigations with twice as many candidates. *Astrophys. J.* **790,** 146 (2014).
8. Agol, E., Steffen, J., Sari, R. & Clarkson, W. On detecting terrestrial planets with timing of giant planet transits. *Mon. Not. R. Astron. Soc.* **359,** 567–579 (2005).
9. Cossou, C., Raymond, S. N., Hersant, F. & Pierens, A. Hot super-Earths and giant planet cores from different migration histories. *Astron. Astrophys.* **569,** A56 (2014).
10. Pu, B. & Wu, Y. Spacing of *Kepler* planets: sculpting by dynamical instability. *Astrophys. J.* **807,** 44 (2015).
11. Chatterjee, S. & Ford, E. B. Planetesimal interactions can explain the mysterious period ratios of small near-resonant planets. *Astrophys. J.* **803,** 33 (2015).
12. Levison, H. F., Morbidelli, A., Tsiganis, K., Nesvorný, D. & Gomes, R. Late orbital instabilities in the outer planets induced by interaction with a self-gravitating planetesimal disk. *Astron. J.* **142,** 152 (2011).
13. Borucki, W. J. *et al.* Characteristics of planetary candidates observed by *Kepler*. II. Analysis of the first four months of data. *Astrophys. J.* **736,** 19 (2011).
14. Lissauer, J. J. *et al.* Architecture and dynamics of *Kepler*'s candidate multiple transiting planet systems. *Astrophys. J. Suppl. Ser.* **197,** 8 (2011).
15. Lissauer, J. J. *et al.* Validation of *Kepler*'s multiple planet candidates. II. Refined statistical framework and descriptions of systems of special interest. *Astrophys. J.* **784,** 44 (2014).
16. Carter, J. A. *et al.* Kepler-36: a pair of planets with neighboring orbits and dissimilar densities. *Science* **337,** 556–559 (2012).
17. Lopez, E. D. & Fortney, J. J. Understanding the mass-radius relation for sub-Neptunes: radius as a proxy for composition. *Astrophys. J.* **792,** 1 (2014).
18. Lee, E. J. & Chiang, E. Breeding super-Earths and birthing super-puffs in transitional disks. *Astrophys. J.* **817,** 90 (2016).
19. Lissauer, J. J. *et al.* A closely packed system of low-mass, low-density planets transiting Kepler-11. *Nature* **470,** 53–58 (2011).
20. Goździewski, K. & Migaszewski, C. Multiple mean motion resonances in the HR 8799 planetary system. *Mon. Not. R. Astron. Soc.* **440,** 3140–3171 (2014).
21. Adams, F. C., Laughlin, G. & Bloch, A. M. Turbulence implies that mean motion resonances are rare. *Astrophys. J.* **683,** 1117–1128 (2008).
22. Masset, F. S., Morbidelli, A., Crida, A. & Ferreira, J. Disk surface density transitions as protoplanet traps. *Astrophys. J.* **642,** 478–487 (2006).
23. Minton, D. A. & Levison, H. F. Planetesimal-driven migration of terrestrial planet embryos. *Icarus* **232,** 118–132 (2014).
24. Ormel, C. W., Ida, S. & Tanaka, H. Migration rates of planets due to scattering of planetesimals. *Astrophys. J.* **758,** 80 (2012).
25. Nelson, B. E. *et al.* An empirically derived three-dimensional Laplace resonance in the Gliese 876 planetary system. *Mon. Not. R. Astron. Soc.* **455,** 2484–2499 (2016).
26. Goździewski, K., Migaszewski, C., Panichi, F. & Szuszkiewicz, E. The Laplace resonance in the Kepler-60 planetary system. *Mon. Not. R. Astron. Soc.* **455,** L104–L108 (2016).
27. Raymond, S. N., Barnes, R., Armitage, P. J. & Gorelick, N. Mean motion resonances from planet-planet scattering. *Astrophys. J.* **687,** L107–L110 (2008).
28. Moore, A., Hasan, I. & Quillen, A. C. Limits on orbit-crossing planetesimals in the resonant multiple planet system, KOI-730. *Mon. Not. R. Astron. Soc.* **432,** 1196–1202 (2013).
29. Batygin, K. & Morbidelli, A. Dissipative divergence of resonant orbits. *Astron. J.* **145,** 1 (2013).
30. Delisle, J.-B. & Laskar, J. Tidal dissipation and the formation of *Kepler* near-resonant planets. *Astron. Astrophys.* **570,** L7 (2014).

METHODS

Stellar properties. To improve our knowledge of the Kepler-223 system, we obtained a spectrum of the host star on 10 April 2012 using the HIRES spectrometer[31] at the Keck-1 10-m telescope. These data are now publicly available at http://cfop.ipac.caltech.edu. After normalizing the continuum, we model the observed spectrum using synthetic spectra. Model spectra are generated by interpolating within a grid of synthetic spectra[32]. The resulting spectroscopic parameters for Kepler-223 are $T_{eff} = 5,821 \pm 123$ K, $\log(g) = 4.070 \pm 0.096$ dex and [Fe/H] $= 0.060 \pm 0.047$ dex (where g is the surface gravity in cm s^{-2} and the metallicity [Fe/H] is the logarithm of the ratio of iron to hydrogen in the star relative to that ratio in the sun).

To determine an age and mass of the star, we match the measured properties to Y^2 isochrones[33]. We ran a Markov chain Monte Carlo (MCMC) using the spectroscopic data and an interpolation of the Y^2 grid values as the model to obtain an age of $6.3^{+1.8}_{-1.7}$ Gyr and mass of $1.125^{+0.095}_{-0.073} M_{\odot}$ (see Extended Data Fig. 1). Combining these values with $\log(g)$, we measure the stellar radius, $R_{\star} = 1.54^{+0.21}_{-0.18} R_{\odot}$, and stellar density, $\rho_{\star} = 0.31^{+0.12}_{-0.09} \rho_{\odot}$. We also derive a distance from Earth to Kepler-223 of $2.29^{+0.34}_{-0.34}$ kpc to Kepler-223 and find the mean flux S on the planets to be $S_b = (492 \pm 47) S_0$, $S_c = (335 \pm 32) S_0$, $S_d = (195 \pm 19) S_0$ and $S_e = (133 \pm 13) S_0$, where $S_0 = 1,377$ W m^{-2} is the average insolation of Earth .

To determine the size of model-dependent uncertainties, we compare our results to an independently developed, publicly available method for computing $M_{\star}$, $R_{\star}$ and age using the Dartmouth isochrones[34] (https://github.com/timothydmorton/isochrones). All three values are consistent within the 1σ error bars, so we conclude that our measurements are robust and that model-dependent errors are small compared to our quoted uncertainties. We also use a stellar population synthesis model, TRILEGAL[35], with the default galaxy stellar distribution and population as described therein, to demonstrate that the best-fit mass and uncertainties described above are essentially unaffected by reasonable priors; so, we keep flat priors for all stellar parameters.

TTVs. To measure TTVs, we begin by detrending the simple aperture photometry (SAP) flux data from the Kepler portal on the Mikulski Archive for Space Telescopes (MAST). For long-cadence data (quarters 1–8), we fit the amplitudes of the first five co-trending basis vectors (largest magnitude vectors from a singular value decomposition of the photometry for a given CCD channel) to determine a baseline. We discard points marked as low quality (quality flag of ≥ 16). For short-cadence data (58.8-s integrations, quarters 9–17), co-trending basis vectors are not available. Instead, we first masked out the expected transit times of a preliminary model, plus 20% of the full duration of each transit intending to account for possible additional timing variations; then we fit a cubic polynomial model with a 2-day width centred within half an hour of each data point to determine its baseline. In both cases, the baseline remains dominated by instrumental systematics that are time-variable; thus, we divide the flux by this baseline.

In computing TTVs, we use only those data for which the transits do not overlap with another planetary transit (that is, two transit mid-times fall within 1 day of each other) according to a preliminary model (data with overlapping transits is modelled directly by the photodynamic method described later). To determine transit times, we first fit transit parameters (period, transit mid-time, planet-to-star radius ratio, transit duration, impact parameter and limb-darkening coefficient) to the entire long-cadence dataset. Second, we refit each quarter using the globally determined values for all parameters except for transit mid-time, which is solved for. Third, we refine the transit shape parameters and slide the refined transit model in time through the data for each planet in each quarter, computing the goodness-of-fit statistic χ^2 in steps of 0.001 days. The values of the numerical χ^2 function that are within 1.0 of the minimum are fit with a parabola, the minimum of which we adopt as our best estimate of the mid-time. The time shifts in each direction at which the χ^2 function rises by 1 and 9 above the minimum are adopted as narrow and conservative error bars. If the likelihood surface of the mid-time parameter was Gaussian, these values would correspond to 1σ and 3σ estimates. Extended Data Table 1 reports the average time of the transits that were combined to make each measurement, the best-estimate and uncertainty estimates of these time shifts. Once phased at these transit times, the transit light curves are shown in Fig. 2. These transit times are also represented graphically in Extended Data Fig. 2 as the horizontal error bar. Planets c, d and e all have visible fluctuations over the dataset. These data constitute our transit timing measurement, which does not depend on the photodynamical model we develop subsequently; also, the data are not used in this model.

We use these transit times to estimate the Laplace critical angles[36] and their evolution. To do so, we note that for circular orbits the mean longitude, λ, is a linear function of time, t, related to the transit period, P, and a specific mid-time, T'_0, as

$$\lambda = 2\pi[1/4 + (t - T'_0)/P]$$

In place of T'_0 we may use $T_0 + \Delta T_0$, where P and T_0 define the linear ephemeris on which the quarterly ΔT_0 of Extended Data Table 1 are based. Then, for Laplace's critical angles we have

$$\phi_1 = -\lambda_b + 2\lambda_c - \lambda_d$$
$$= 2\pi \left[\frac{T'_{0b}}{P_b} - \frac{2T'_{0c}}{P_c} + \frac{T'_{0d}}{P_d} + t\left(\frac{2}{P_c} - \frac{1}{P_b} - \frac{1}{P_d} \right) \right]$$
$$= 2\pi \left[0.4750 + 2.39834 \times 10^{-5}(t - 2,454,900) + \frac{\Delta T_{0b}}{P_b} - \frac{2\Delta T_{0c}}{P_c} + \frac{\Delta T_{0d}}{P_d} \right]$$

where t is given in units of days in terms of the barycentric Julian date (BJD), and similarly

$$\phi_2 = \lambda_c - 3\lambda_d + 2\lambda_e$$
$$= 2\pi \left[-\frac{T'_{0c}}{P_c} + \frac{3T'_{0d}}{P_d} - \frac{2T'_{0e}}{P_e} + t\left(\frac{1}{P_c} - \frac{3}{P_d} + \frac{2}{P_e} \right) \right]$$
$$= 2\pi \left[0.1135 + 8.7366 \times 10^{-5}(t - 2,454,900) - \frac{\Delta T_{0c}}{P_c} + \frac{3\Delta T_{0d}}{P_d} - \frac{2\Delta T_{0e}}{P_e} \right]$$

These values are plotted in Extended Data Fig 3. The values are not constant, and the data appear to have sampled a minimum and maximum value of a libration cycle, which indicates a restoring torque. The specific values are sensitive to phase shifts due to eccentricity-vector precession; the libration centres may be different by about 30° if the eccentricities are as high as 0.1.

Photodynamic inputs. A Newtonian photodynamic model similar to existing models[37], but developed independently, was used for a dynamical analysis of this system. To find the most likely parameter values and uncertainties in the system, we run a differential-evolution Markov chain Monte Carlo (DEMCMC)[38] to compare model output for different system parameters to observed long- and short-cadence Kepler data, as well as spectroscopic data of the star. The TTV signal (Fig. 1), which here is constrained by the photometry directly, detects the gravitational perturbations due to planet mass. Combined with transit shape information, this constrains the eccentricities and provides positive mass detections at $>2.5\sigma$ for all bodies with uncertainties approximately 10–30% of the fitted values.

Each planet ($i = $ b, c, d, e) has seven parameters: $\boldsymbol{p}_i = [P, T_0, e\cos(\omega), e\sin(\omega), i, \Omega, R_p/R_{\star}, M_p/M_{\star}]$ in which P is the period, T_0 is the mid-transit time, e is the eccentricity, i is the inclination, ω is the argument of periastron, Ω is the nodal angle, $R_p/R_{\star}$ is the planet-to-star radius ratio and $M_p/M_{\star}$ is the planet-to-star mass ratio. The star has five parameters: $\boldsymbol{p}_{\star} = [M_{\star}, R_{\star}, c_1, c_2, \text{dilution}]$, in which c_i are the two quadratic limb-darkening coefficients and 'dilution' is the amount of dilution from other stars. Because photometry constrains only stellar density, and not mass and radius individually, we fix $M_{\star}$ at the best-fit value found from spectroscopy and convolve the mass distribution with the DEMCMC posteriors when reporting final values.

We fix $\Omega = 0$ for all planets because the data do not sensitively measure mutual inclinations. The typical mean mutual inclination (MMI) of Kepler systems, approximately 1.8°, implies near coplanarity[7]. Additionally, multi-planet systems with higher mutual inclinations between planetary orbital planes are correlated with instability[39], and we expect any observed system to be at least quasi-stable. Although, for some pairs of planets, photometry determines whether their inclinations are on the same side of 90° (refs 40, 41), in preliminary runs we find no preference for either conclusion. Therefore, we explore only $i > 90°$ for each planet to reduce the volume of the symmetric parameter space. The value for the stellar limb-darkening coefficient c_2 was chosen as 0.2 because this value is close to the median value for stars in the 4,000–6,500-K range in the Kepler bandpass[42], and for low signal-to-noise ratio transits such as that in Kepler-223, a single limb-darkening parameter is sufficient to match transit shape[43,44].

United Kingdom Infrared Telescope (UKIRT) archives reveal that there are two objects within 2″ of the position specified by the Kepler Input Catalog (KIC)[45]. The brighter of the two objects is less than 0.2″ from the KIC position and has a predicted Kepler magnitude of 15.4932, which is based on the formula used within the UKIRT archives to convert the measured J-band magnitudes to a Kepler magnitude[46]. This value is 0.1492 magnitudes fainter than that reported in the KIC (15.344). The second object is 1.937″ away from the KIC location, but is about 8 times fainter. The sum of these two objects has a predicted intensity in the Kepler bandpass equal to 98.2% of the intensity of the object reported by the KIC. Faulkes Telescope North (FTN) imaging confirms the dual nature of the Kepler-223 object[47]. Speckle imaging done at WIYN observatory indicates no additional bodies between approximately 0.2″ and 1.9″ of the brighter object[48]. Because the fainter of the two objects contributes approximately 11.202% of the light in the Kepler bandpass, we perform our DEMCMC runs with the dilution fixed at 0.11202.

Photodynamic fits. Beginning the DEMCMC by distributing parameters over the entire 30-dimensional prior is computationally untenable for this problem because it would take an excessively long time for the parameter sets, $\{p_i\}$, of the DEMCMC to escape local minima and reach the global minimum. Instead we begin the DEMCMC by taking a four-planet solution found by exploration using migration-assembly solutions, p_0, which approximately matches the observed data, and forming a set of 48 30-parameter vectors, $\{p_0\}$, by adding 30-dimensional Gaussian noise to p_0. We allow each set to explore the parameter space and, to eliminate any effects of the choice of p_0, we wait until the DEMCMC chains have converged and then remove a 'burn-in' period, that is, the portion that is dependent on the choice of $\{p_0\}$.

In the DEMCMC, a given choice of planetary parameters is accepted or rejected one the basis of the data over the Kepler observing window (about 4 years), and does not take into account the long-term evolution of a system with such parameters. It is not computationally tenable to numerically integrate each model for the age of the Kepler-223 system during the DEMCMC run. Therefore, the DEMCMC posterior includes solutions that acceptably fit the data, but that become unstable shortly after. To prevent our posterior parameter estimates from representing unstable solutions, we take two steps to encourage stability. First, we do not allow the DEMCMC to explore any solutions where the orbits of two adjacent planets cross (which generates a posterior we call $\mathcal{C}_1$). This was implemented by allowing the DEMCMC to explore a limited range of eccentricities for each planet, $(e_{b,max}, e_{c,max}, e_{d,max}, e_{e,max}) = (0.212, 0.175, 0.212, 0.175)$, with the symmetry of values due to the resonant-chain structure of the periods (posteriors can be found in Extended Data Table 2 and best-fits in Extended Data Table 3). Retrospectively, this eccentricity prior is justified because mean eccentricities greater than 0.1 are very rarely stable (Extended Data Fig. 6). Further, the similarity between the 10^6-year eccentricity-stability distribution and the 10^7-year distribution indicates that using either as a proxy for stable solutions will yield comparable results.

To assess the stability of the solutions in the posterior distribution, we selected 500 random draws from the $\mathcal{C}_1$ posterior and numerically integrated each of these solutions for 10^7 years, which corresponds to more than 10^8 orbits of the outermost planet. We used the MERCURY symplectic integrator[49] and stopped integration if a close encounter between any two bodies occurred. 30% of systems lasted the entire 10^7-year integration. We randomly selected 25 of the systems that lasted 10^7 years and numerically integrated them for an additional 9×10^7 years, or until a close encounter, with 64% of them lasting 10^8 years. The age of the Kepler-223 star is about 6×10^9 years. We expect the planets to have reached their current configuration by migration through a disk within only a few million years, which corresponds to the lifetimes of gas disks[50], suggesting that the current planet configuration has also survived for about 6×10^9 years. However, integrating for this long is not computationally feasible for this study. Other numerical stability studies[10] predict that systems are approximately equally likely to become unstable in bins of log(time), implying that approximately 12% of the tested systems (and thus approximately 12% of the systems in the $\mathcal{C}_1$ posterior) remain stable on timescales of billions of years . This fraction is high compared to a modelled population of compact, sub-Neptune systems, which are destabilized by mean motion resonances (MMRs) on a shorter timescale[10]. However, in such simulations there are generally a few bodies not engaged in the resonance; here all four bodies are involved in the resonance, remaining stable despite MMRs exciting eccentricities. Also, MERCURY is a Newtonian physics integrator, but adding a suitable general relativistic potential term, $U_{GR} = -3(GM_\star/(cr))^2$, where G is the gravitational constant, c is the speed of light and r is the distance from a planet to the star[51], does not change our long-term stability results from 100 trials (32 stable, 68 unstable).

To develop a second posterior based on parameters that are more likely to lead to stability, we randomly drew 5,000 parameter sets from the posterior of $\mathcal{C}_1$, and numerically integrated each of these solutions for 10^6 years (corresponding to more than 10^7 orbits of the outermost planet). This allows the problem to be computationally feasible, while still allowing for a large enough number of draws that we have sufficient statistics for parameter estimates. We retained only those parameter sets that remained stable at least this long (2,008 in total) to form a second posterior representative of physical (stable) solutions and call it $\mathcal{C}_2$. Future discussions of parameters and the data in the main text (Table 1 and Fig. 1) use this posterior ($\mathcal{C}_2$) because we judge it to be the optimal combination of selecting stable solutions that match the observed Kepler data, while avoiding discarding plausible parameter space as a result of further assumptions. The general shape of the eccentricity distribution remaining after 10^6 years does not change markedly compared to solutions that are stable for an order of magnitude longer (see Extended Data Fig. 6) and is thus unlikely to change noticeable over the ~6-Gyr age of the system. The instability regions near the best-fit values discovered by our parameter fits suggest the ease with which the system, and others like it, could

be moved out of resonance by small perturbations such as evaporation of the protoplanetary disk[9,28].

Kepler-223 appears to possess two librating Laplace angles between the inner three and outer three planets, as discussed earlier. Migration simulations suggest that a very large Laplace-angle libration amplitude is unlikely in stable solutions. Further, in stable solutions in the $\mathcal{C}_2$ posterior, long-lived (up to about 10^5 years) Laplace-angle libration is likely to occur. To get another estimate of the parameters of the system while balancing computational efficiency and a stricter stability constraint, we ran a third DEMCMC. For this run, at every step in the DEMCMC we integrate the parameter initial conditions for 100 years (corresponding to more than about 5 secular oscillations) and penalize Laplace-angle oscillation amplitudes that grow too large, in addition to fitting the data. We call the posterior from this run $\mathcal{C}_3$. Our Laplace-angle criteria in $\mathcal{C}_3$ are designed to penalize large libration amplitudes and the speed at which the amplitudes grow. If the total range in Laplace angles, $\Delta\phi_1$ or $\Delta\phi_2$, exceeds a cut-off value K_1 over the integration time (T_{max}, in years), then the time at which this occurs is recorded ($T_{runaway}$). A value $-1 + (T_{runaway}/T_{max})^{-2}$ is added to the χ^2 value. All χ^2 values were also penalized by an additional term equal to $(\Delta\phi - V_i)^2$ if $\Delta\phi_i > V_i$ and to 0 if $\Delta\phi_i < V_i$ for specified angles V_i, $i = 1, 2$, in degrees and with $\Delta\phi = \phi_{max} - \phi_{min}$. This way, if the Laplace angles were well behaved enough not to run away, but either or both still grew in amplitude above specified values for each angle (V_1 and V_2), then a χ^2 penalty was assigned and the parameters were less likely to be accepted. We do not impose a direct eccentricity constraint. We report $\mathcal{C}_3$ with $(T_{max}, K_1, V_1, V_2) = (100 \text{ yr}, 170°, 30°, 50°)$, for which the numbers are roughly based on the results of migration and DEMCMC results that had long-term libration (see Extended Data Table 2).

Running a similar stability check for $\mathcal{C}_3$ as for $\mathcal{C}_1$ by choosing 300 chains from the posterior distribution resulted in 100% of the parameter sets leading to stable behaviour lasting 10^7 years. Ten parameter sets were numerically integrated for 10^8 years, and 100% of those also lead to a system that survives with no close encounters. These results indicate that this method is effective at finding stable solutions. Comparing this to the stability results for $\mathcal{C}_1$, in which only 19% of solutions were stable for 10^8 years (as described above), our argument that resonance does encourage stability is strengthened. Nevertheless, this method cannot be guaranteed to reject all unstable systems (because they might pass this test) or to include all stable ones (because some systems could remain stable for a very long time, but have large changes in Laplace angle; see Extended Data Fig. 4). This posterior has lower eccentricities, but because we assume short-term resonance for this fit, we do not take it as our nominal fit.

Future observations. We predict future transit times and uncertainties by averaging the predicted transits from 152 solutions from the $\mathcal{C}_1$ posterior that are stable for 10^7 years. We report transit times quarterly for 10 years, including over the Kepler observing window, in Supplementary Information.

Code availability. The code used for migration simulations is available as Supplementary Information. The code used to generate the TTV and photodynamic analyses is available upon request and will be made publicly available once further analyses have been completed.[50]

31. Vogt, S. S. *et al.* HIRES: the high-resolution echelle spectrometer on the Keck 10-m Telescope. *Proc. SPIE* **2198,** 362–375 (1994).
32. Coelho, P., Barbuy, B., Melndez, J., Schiavon, R. P. & Castilho, B. V. A library of high resolution synthetic stellar spectra from 300 nm to 1.8 μm with solar and α-enhanced composition. *Astron. Astrophys.* **443,** 735–746 (2005).
33. Demarque, P., Woo, J.-H., Kim, Y.-C. & Yi, S. K. Y^2 isochrones with an improved core overshoot treatment. *Astrophys. J. Suppl. Ser.* **155,** 667–674 (2004).
34. Morton, T. D. isochrones: stellar model grid package. *Astrophysics Source Code Library* ascl:1503.010, http://ascl.net/1503.010 (2015).
35. Girardi, L., Groenewegen, M. A. T., Hatziminaoglou, E. & da Costa, L. Star counts in the Galaxy. Simulating from very deep to very shallow photometric surveys with the TRILEGAL code. *Astron. Astrophys.* **436,** 895–915 (2005).
36. Quillen, A. C. Three-body resonance overlap in closely spaced multiple-planet systems. *Mon. Not. R. Astron. Soc.* **418,** 1043–1054 (2011).
37. Carter, J. A. *et al.* KOI-126: a triply eclipsing hierarchical triple with two low-mass stars. *Science* **331,** 562–565 (2011).
38. ter Braak, C. J. F. *Genetic Algorithms and Markov Chain Monte Carlo: Differential Evolution Markov Chain Makes Bayesian Computing Easy.* Report No. 010404 (revised) http://edepot.wur.nl/39477 (Biometris, 2005).
39. Veras, D. & Armitage, P. J. The dynamics of two massive planets on inclined orbits. *Icarus* **172,** 349–371 (2004).
40. Huber, D. *et al.* Stellar spin-orbit misalignment in a multiplanet system. *Science* **342,** 331–334 (2013).
41. Masuda, K., Hirano, T., Taruya, A., Nagasawa, M. & Suto, Y. Characterization of the KOI-94 system with transit timing variation analysis: implication for the planet-planet eclipse. *Astrophys. J.* **778,** 185 (2013).
42. Sing, D. K. Stellar limb-darkening coefficients for CoRot and Kepler. *Astron. Astrophys.* **510,** A21 (2010).

43. Southworth, J., Bruntt, H. & Buzasi, D. L. Eclipsing binaries observed with the WIRE satellite. II. β Aurigae and non-linear limb darkening in light curves. *Astron. Astrophys.* **467,** 1215–1226 (2007).

44. Southworth, J. Homogeneous studies of transiting extrasolar planets – I. Light-curve analyses. *Mon. Not. R. Astron. Soc.* **386,** 1644–1666 (2008).

45. Brown, T. M., Latham, D. W., Everett, M. E. & Esquerdo, G. A. *Kepler* input catalog: photometric calibration and stellar classification. *Astron. J.* **142,** 112 (2011).

46. Howell, S. B. *et al.* Kepler-21b: a 1.6 R_{Earth} planet transiting the bright oscillating F subgiant star HD 179070. *Astrophys. J.* **746,** 123 (2012).

47. Brown, T. M. *et al.* Las Cumbres Observatory Global Telescope network. *Publ. Astron. Soc. Pacif.* **125,** 1031–1055 (2013).

48. Howell, S. B., Everett, M. E., Sherry, W., Horch, E. & Ciardi, D. R. Speckle camera observations for the NASA *Kepler* mission follow-up program. *Astron. J.* **142,** 19 (2011).

49. Chambers, J. E. Mercury: a software package for orbital dynamics. *Astrophysics Source Code Library* ascl:1201.008, http://ascl.net/1201.008 (2012).

50. Williams, J. P. & Cieza, L. A. Protoplanetary disks and their evolution. *Annu. Rev. Astron. Astrophys.* **49,** 67–117 (2011).

51. Lissauer, J. J. *et al.* Architecture and dynamics of *Kepler*'s candidate multiple transiting planet systems. *Astrophys. J. Suppl. Ser.* **197,** 8 (2011).

52. Batalha, N. M. *et al.* Planetary candidates observed by *Kepler*. III. Analysis of the first 16 months of data. *Astrophys. J. Suppl. Ser.* **204,** 24 (2013).

Y^2 evolution tracks and observed stellar parameters

1.18 Msun, 6.0 Gyr
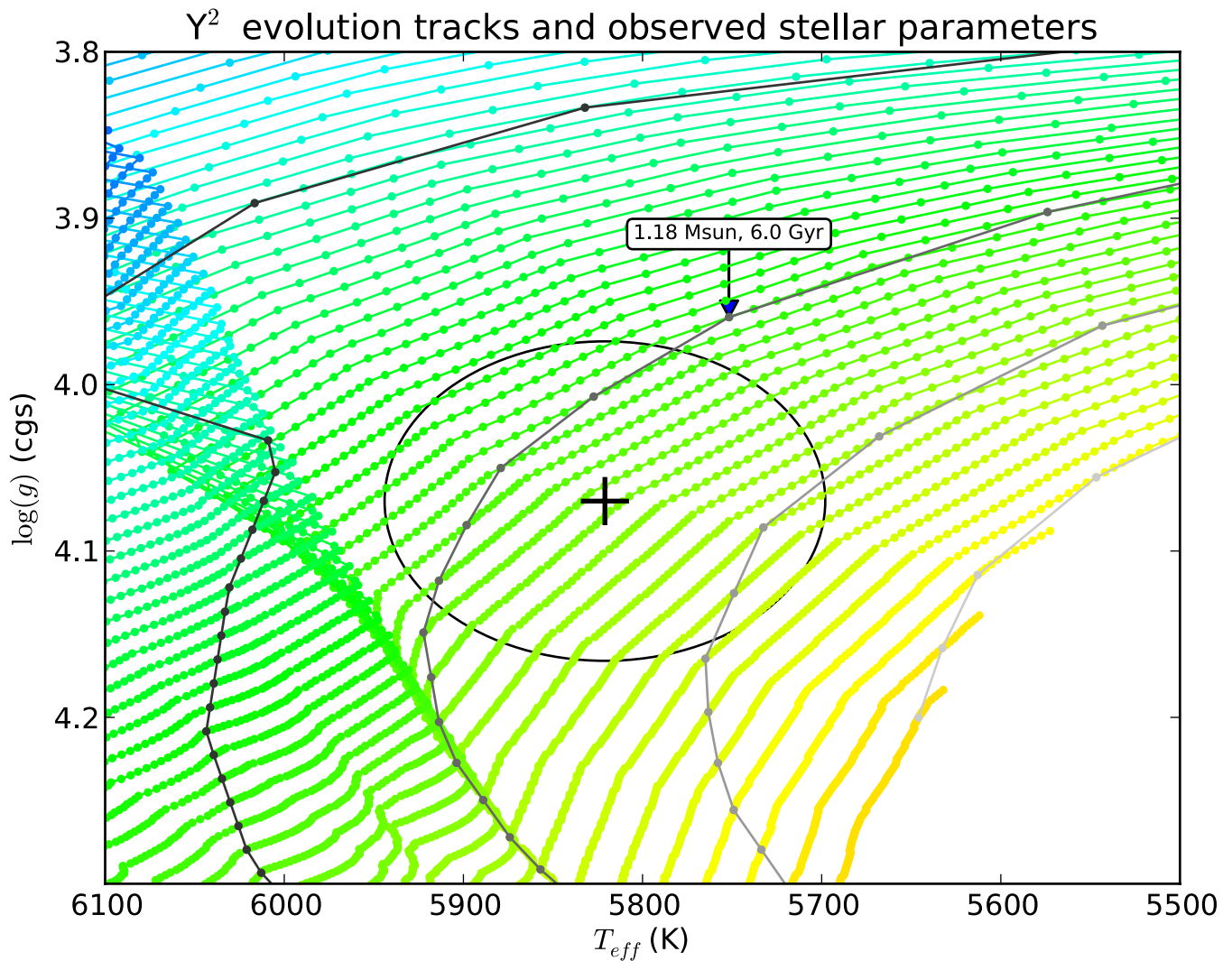
Extended Data Figure 1 | Spectroscopic fit of the Kepler-223 star.
A fit to Yonsei–Yale (Y^2) evolution tracks (coloured lines) with 0.01-Gyr increments marked with filled circles. Colours correspond to mass with increments of $0.01M_\odot$ from $1.0M_\odot$ (orange) to $1.4M_\odot$ (darkest blue). Isochrones (grey lines) are over-plotted in 2-Gyr increments from 4 Gyr (darkest grey) to 10 Gyr (lightest grey) with filled circles every $0.01M_\odot$ increment. One point is labelled for reference ($Msun = M_\odot$). The best-fit (T_{eff}, $\log(g)$) value (black cross) and an ellipse (black) whose semi-major axes indicate 1σ uncertainties of each parameter found from spectral matching are indicated. The stars in this area of parameter space have evolved off the main sequence.
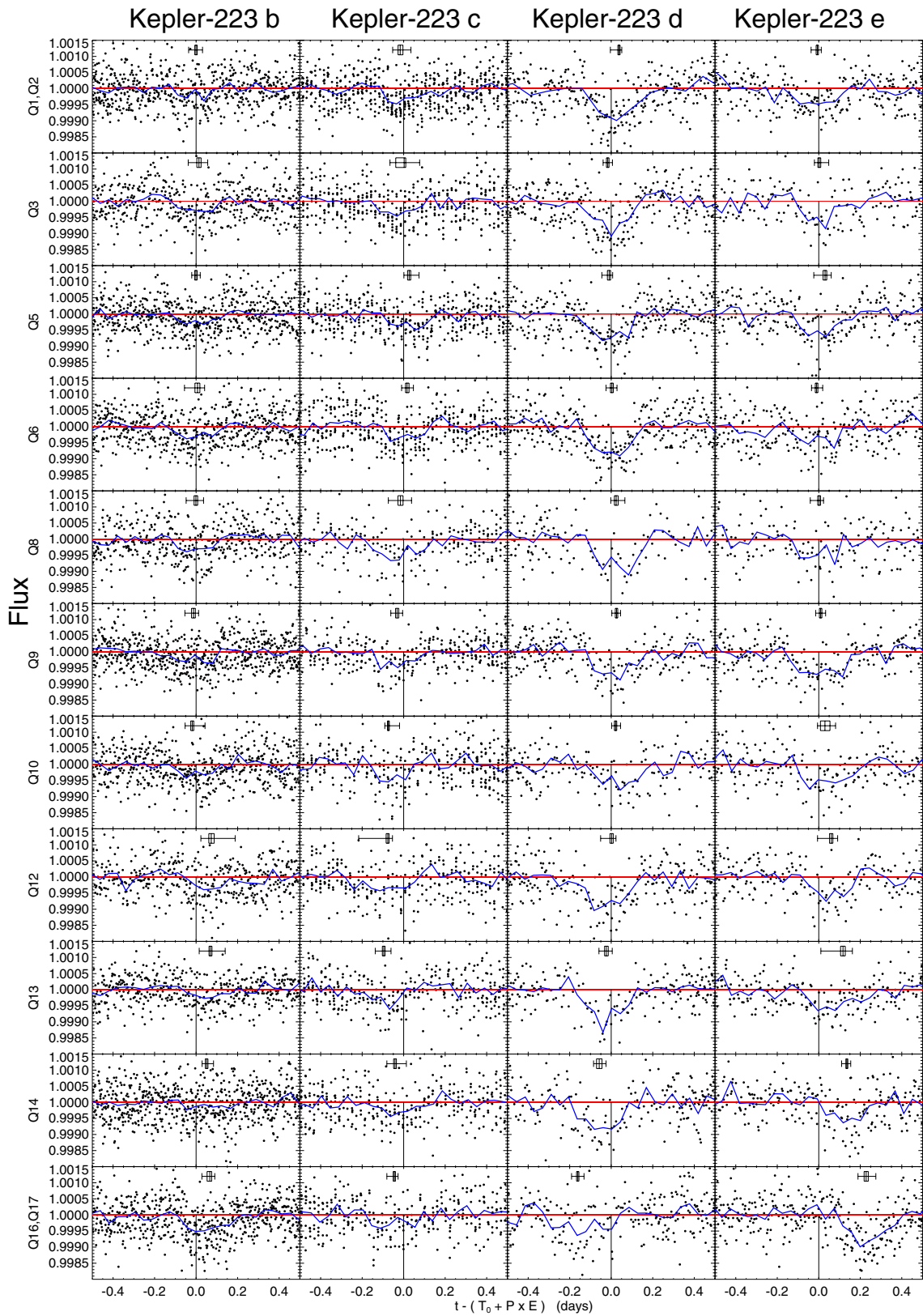
Extended Data Figure 2 | Long-cadence light curve for each planet, broken down by quarter (Q). Data (black filled circles) are binned via a moving average to give the blue curve, to reduce the scatter relative to the horizontal red line indicating no signal. Each panel is centred on the transit times predicted using the linear ephemeris (T_0 and P) of ref. 52 (vertical black lines), with the horizontal axis the time in days from the Eth predicted transit time. The box-and-whisker error bars indicate the best-fit mid-transit time and 1σ and 3σ uncertainties based on $\Delta\chi^2 = 1$ and $\Delta\chi^2 = 9$. χ^2 values are computed by sliding an overall fit to the transit horizontally across the data and interpolating. Their offset relative to the linear ephemeris lines indicates the magnitudes of the TTVs.
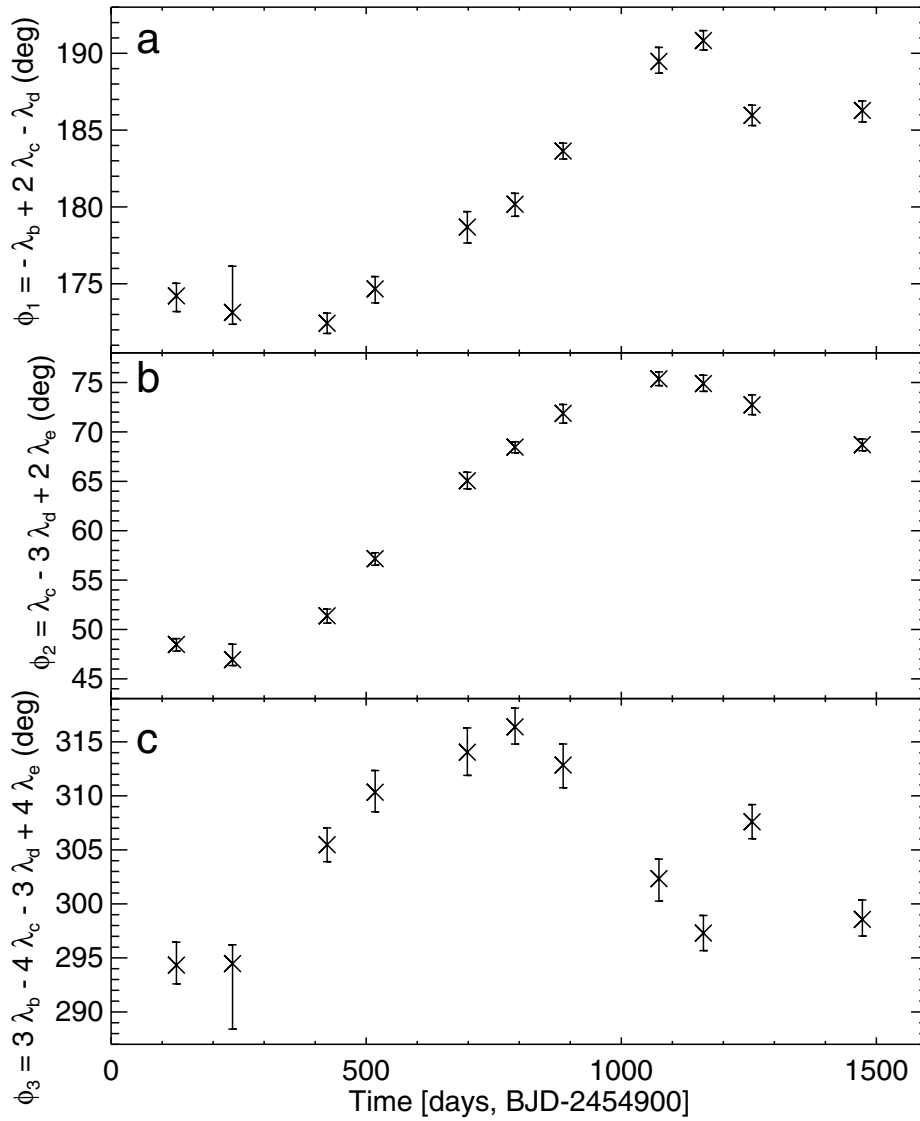
Extended Data Figure 3 | Laplace-angle librations detected by binning transits into quarters and assuming zero eccentricity. a–c, Error bars show 1σ uncertainties based on $\Delta\chi^2 = 1$. Almost a full libration cycle of all angles is observed in the ~1,500-day observing window. The amplitude of oscillation in the four-body Laplace angle (ϕ_3; **c**) is similar in amplitude to each of the individual Laplace angles (ϕ_1, **a**; ϕ_2, **b**). Because $\phi_3 = -3\phi_1 + 2\phi_2$, this amplitude could naively be expected to be much larger; however, ϕ_1 and ϕ_2 are closely related, owing to the four-body resonance of the Kepler-223 system, in contrast to two independent three-body resonances.
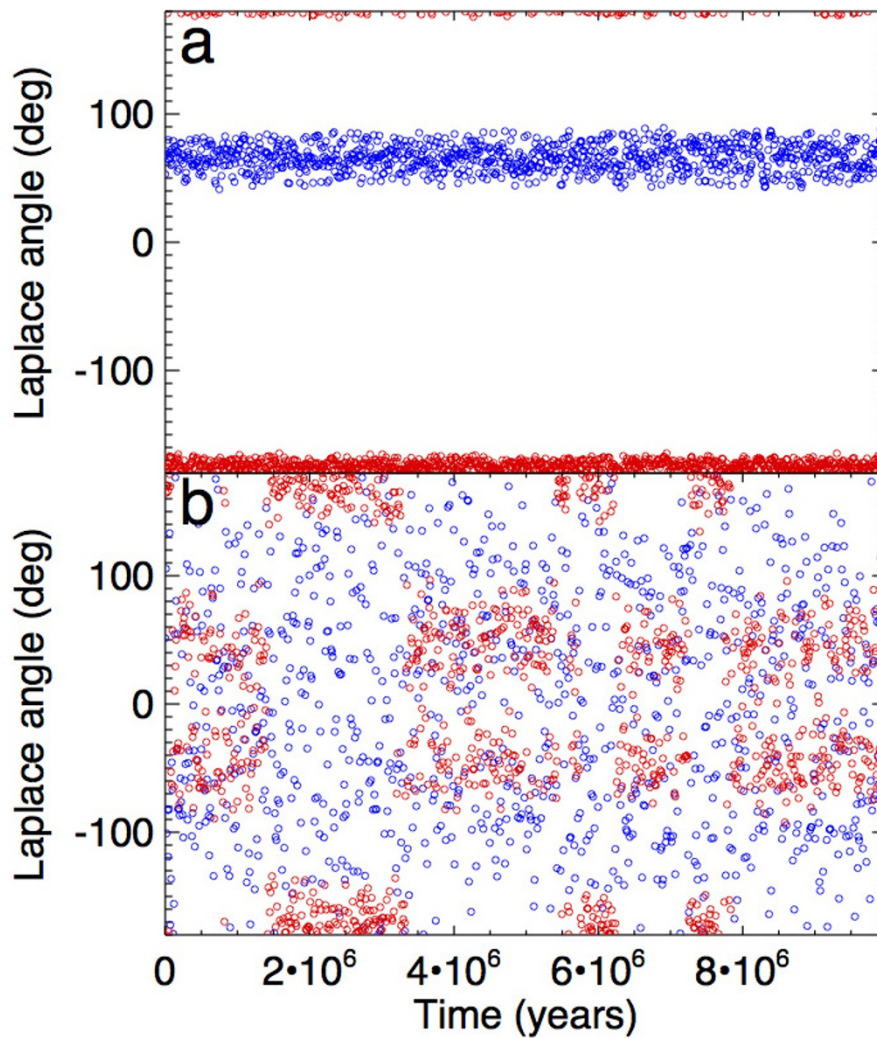
Extended Data Figure 4 | Variation in Laplace angles for two 10^7-year-stable solutions. a, The librating Laplace angles (ϕ_1, red; ϕ_2, blue) for a solution from the $\mathcal{C}_3$ DEMCMC posterior. Laplace angles librate over the entire 10^7 years. The orbital-period distribution in Extended Data Fig. 5 uses this model. **b**, Another solution from $\mathcal{C}_3$, in which the inner Laplace angle (ϕ_1; red) librates near the observed value initially, but begins switching chaotically between three different libration centres. This is not uncommon in the $\mathcal{C}_3$ DEMCMC posterior. Despite the initial constraint on the outer Laplace angle (ϕ_2; blue), there are long periods of circulation with intermittent libration.
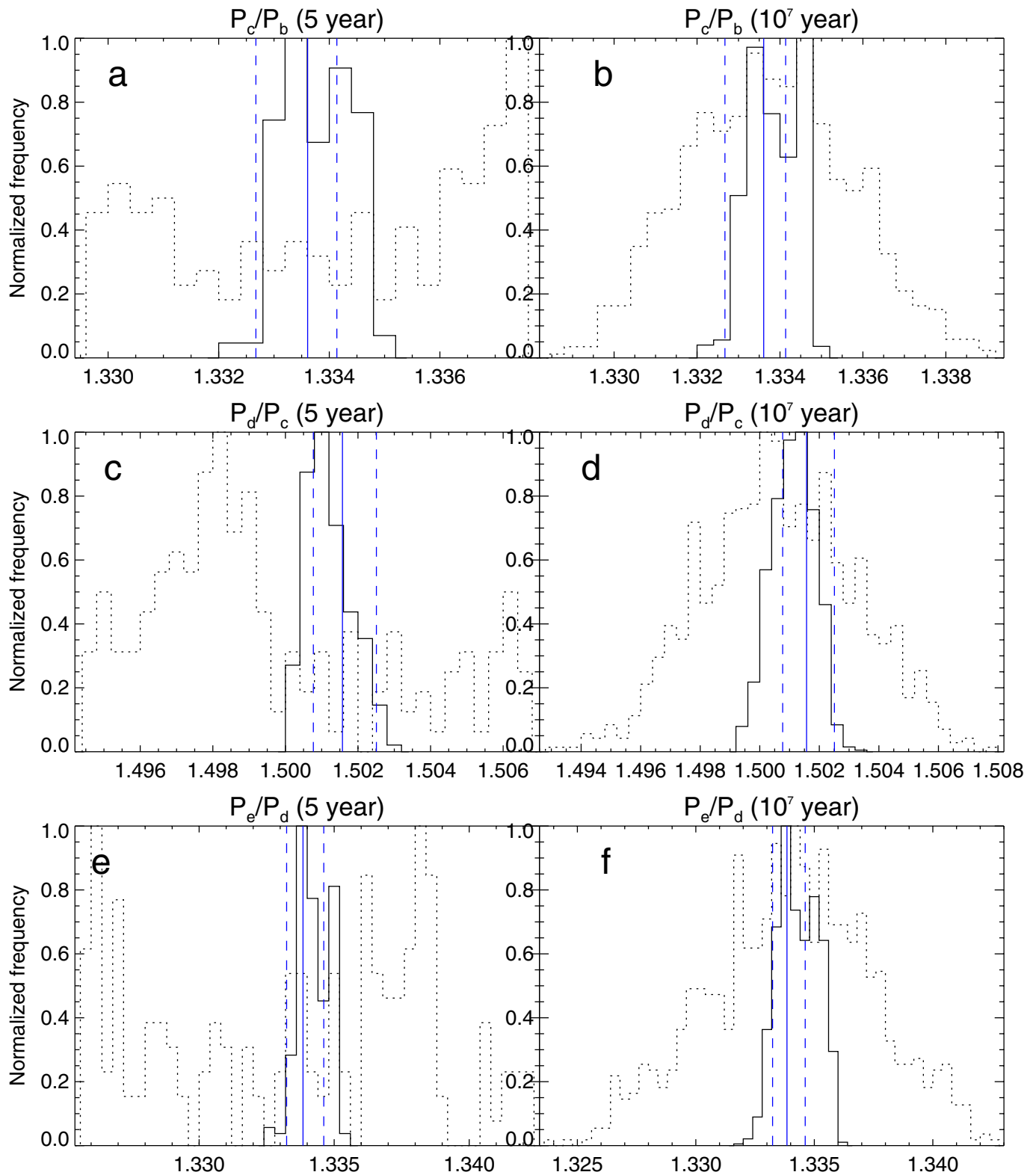
Extended Data Figure 5 | Orbital-period ratios of librating and non-librating solutions fitted to data. a, c, e, The distribution of osculating period ratios for each neighbouring planet pair (P_c/P_b, **a**; P_d/P_c, **c**; P_e/P_d, **e**) over a randomly selected 4-year window in the first 10^4 years for two 10^7-year-stable parameter sets from the $\mathcal{C}_3$ DEMCMC posterior solution. The dotted histogram represents a solution that showed substantial periods of Laplace-angle circulation. The solid histogram represents a solution in which both ϕ_1 and ϕ_2 librate for 10^7 years. The blue vertical line indicates the empirical mean period; blue dashed vertical lines represent the highest and lowest quarter-to-quarter period measured. **b, d, f,** The same as in **a, c, e,** but over the entire 10^7-year interval.
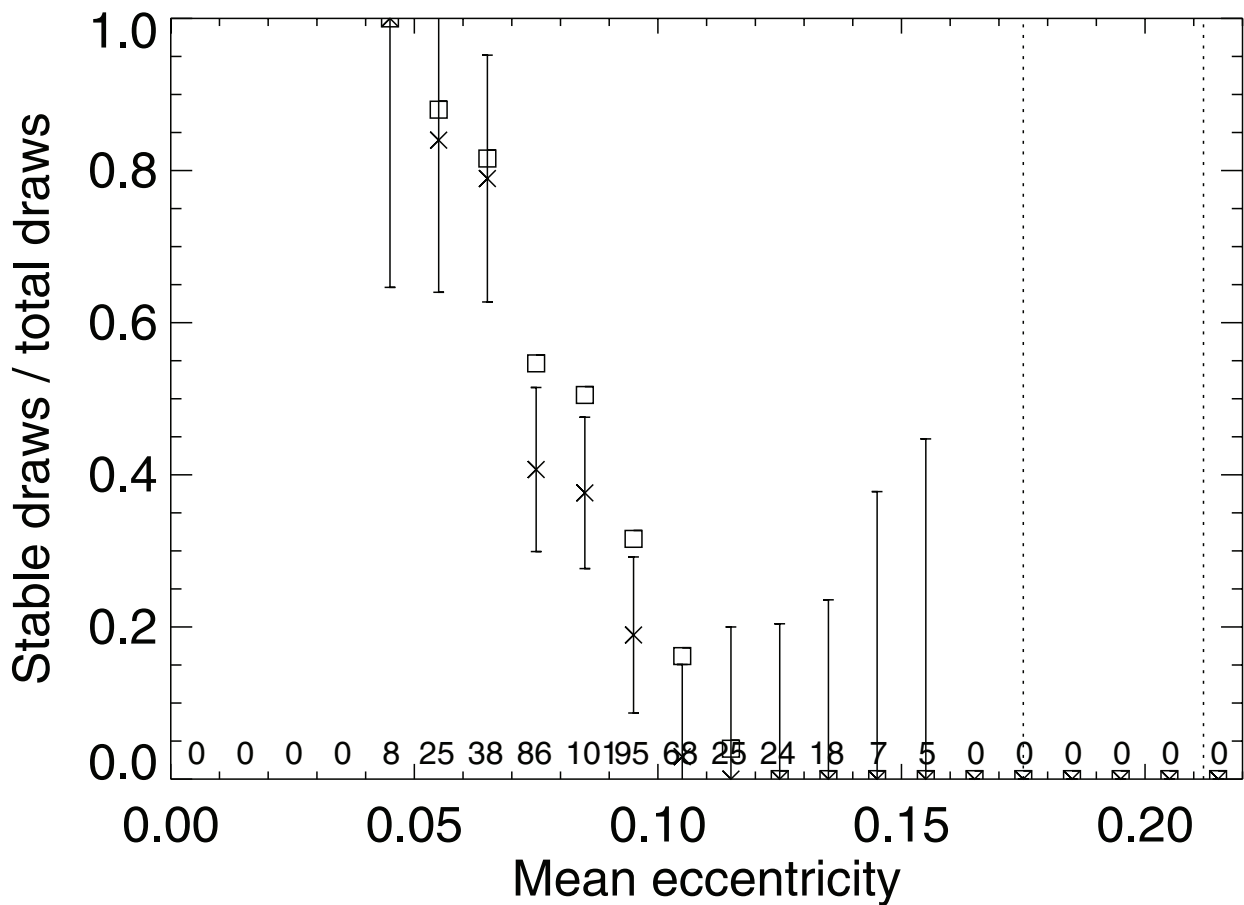
Extended Data Figure 6 | System stability as a function of mean planetary eccentricity. The fraction of 500 random draws from the $\mathcal{C}_1$ posterior that survive for 10^7 years (crosses) and 10^6 years (squares) as a function of four-planet-mean eccentricity in bins of width 0.01. 1σ statistical uncertainties are included as vertical error bars on the crosses. Dotted lines indicate the two eccentricity limits for the planets used in $\mathcal{C}_1$: 0.175 (planets c and e) and 0.212 (planets b and d). Numbers represent the total number of draws in each eccentricity bin. The fraction of 10^7-year-stable systems falls sharply and is consistent with zero well below the eccentricity cuts imposed by $\mathcal{C}_1$.

Extended Data Table 1 | Mean Kepler-223 quarterly TTVs

$\bar{t} - 2454900$ (BJD)	-3σ	$-\sigma$	Best	$+\sigma$	$+3\sigma$
Kepler-223b: P = 7.3840154 days, $T_0 - 2454900$ (BJD) = 70.49489					
123.32662	-0.0354	-0.0058	-0.0006	0.0059	0.0316
239.02516	-0.0517	-0.0103	0.0137	0.0101	0.0423
416.51724	-0.0200	-0.0061	-0.0010	0.0062	0.0210
521.69775	-0.0628	-0.0123	0.0068	0.0113	0.0342
699.18988	-0.0470	-0.0088	-0.0010	0.0084	0.0370
797.79657	-0.0417	-0.0097	-0.0123	0.0088	0.0243
886.54260	-0.0343	-0.0072	-0.0187	0.0074	0.0617
1073.89526	-0.0500	-0.0118	0.0730	0.0140	0.1150
1162.64136	-0.0542	-0.0071	0.0692	0.0071	0.0708
1251.38745	-0.0217	-0.0062	0.0507	0.0065	0.0333
1458.46155	-0.0379	-0.0129	0.0659	0.0090	0.0241
Kepler-223c: P = 9.8487130 days, $T_0 - 2454900$ (BJD) = 71.37624					
116.10564	-0.0362	-0.0103	-0.0168	0.0133	0.0518
242.86336	-0.0683	-0.0405	0.0023	0.0077	0.0747
420.32413	-0.0254	-0.0077	0.0264	0.0076	0.0476
509.05453	-0.0266	-0.0077	0.0166	0.0090	0.0304
701.30371	-0.0585	-0.0121	-0.0155	0.0126	0.0535
790.03418	-0.0302	-0.0075	-0.0318	0.0084	0.0268
886.15869	-0.0173	-0.0046	-0.0737	0.0048	0.0537
1071.01367	-0.1404	-0.0078	-0.0766	0.0066	0.0226
1148.65283	-0.0411	-0.0067	-0.0959	0.0064	0.0349
1252.17163	-0.0392	-0.0067	-0.0418	0.0068	0.0548
1470.30054	-0.0361	-0.0056	-0.0449	0.0051	0.0179
Kepler-223d: P = 14.7883997 days, $T_0 - 2454900$ (BJD) = 109.76775					
132.10997	-0.0416	-0.0058	0.0376	0.0054	0.0134
248.65308	-0.0221	-0.0062	-0.0169	0.0063	0.0229
427.57138	-0.0351	-0.0084	-0.0099	0.0070	0.0169
519.49268	-0.0285	-0.0070	0.0035	0.0066	0.0245
711.54260	-0.0260	-0.0086	0.0240	0.0094	0.0420
800.18097	-0.0226	-0.0060	0.0256	0.0057	0.0194
898.66815	-0.0192	-0.0057	0.0212	0.0055	0.0238
1077.35193	-0.0530	-0.0080	0.0020	0.0077	0.0210
1169.50781	-0.0354	-0.0085	-0.0236	0.0093	0.0286
1271.27771	-0.0272	-0.0131	-0.0578	0.0132	0.0328
1483.43542	-0.0298	-0.0061	-0.1612	0.0057	0.0302
Kepler-223e: P = 19.7213435 days, $T_0 - 2454900$ (BJD) = 68.10686					
135.47421	-0.0303	-0.0060	-0.0067	0.0053	0.0187
238.21753	-0.0232	-0.0067	0.0022	0.0072	0.0458
433.78842	-0.0542	-0.0095	0.0302	0.0084	0.0298
524.27625	-0.0244	-0.0061	-0.0106	0.0063	0.0296
709.21222	-0.0432	-0.0071	0.0022	0.0065	0.0208
797.82037	-0.0240	-0.0060	0.0090	0.0061	0.0240
893.81256	-0.0357	-0.0216	0.0297	0.0242	0.0513
1079.88989	-0.0662	-0.0083	0.0602	0.0078	0.0308
1170.71301	-0.1067	-0.0118	0.1167	0.0110	0.0453
1263.01343	-0.0252	-0.0049	0.1352	0.0049	0.0188
1469.48169	-0.0393	-0.0097	0.2283	0.0100	0.0467

Transit times and TTVs (in days) for each planet found by binning the data quarterly and iteratively solving for transit shape as described in Methods. Mean transit time in the quarter is given in the first column followed by the measured TTV and uncertainties as described in Extended Data Fig. 2.

Extended Data Table 2 | Complete Kepler-223 parameters

Parameter Name (Unit)	Eccentricity Prior ($\mathcal{C}1$)	Eccentricity Prior and Stability ($\mathcal{C}2$)	Laplace Angle Constraint ($\mathcal{C}3$)
Stellar Parameters:			
$R_\star (R_\odot)$	$1.714^{+0.079}_{-0.165}$	$1.72^{+0.07}_{-0.14}$	$1.622^{+0.078}_{-0.070}$
$M_\star (M_\odot)$	1.125 (fixed)	1.125 (fixed)	1.125 (fixed)
c_1	$0.54^{+0.11}_{-0.10}$	$0.54^{+0.10}_{-0.09}$	$0.57^{+0.11}_{-0.10}$
c_2	0.2 (fixed)	0.2 (fixed)	0.2 (fixed)
dilution	0.11202 (fixed)	0.11202 (fixed)	0.11202 (fixed)
Kepler-223 b Parameters:			
P (d)	$7.38454^{+0.00024}_{-0.00028}$	$7.38449^{+0.00022}_{-0.00022}$	$7.38453^{+0.00024}_{-0.00024}$
T_0 (BJD-2454900)	$801.5145^{+0.0044}_{-0.0047}$	$801.5155^{+0.0044}_{-0.0046}$	$801.5133^{+0.0042}_{-0.0045}$
$e \cdot \cos(\omega)$	$0.057^{+0.034}_{-0.031}$	$0.054^{+0.022}_{-0.022}$	$0.035^{+0.014}_{-0.016}$
$e \cdot \sin(\omega)$	$0.052^{+0.026}_{-0.135}$	$0.047^{+0.020}_{-0.039}$	$-0.004^{+0.029}_{-0.034}$
$\|i - 90\|$ (°)	$0.0^{+1.7}$	$0.0^{+1.8}$	$0.0^{+1.4}$
Ω (°)	0.0 (fixed)	0.0 (fixed)	0.0 (fixed)
$M/M_\star$	$0.0000196^{+0.0000034}_{-0.0000031}$	$0.0000221^{+0.0000032}_{-0.0000031}$	$0.0000201^{+0.0000027}_{-0.0000026}$
$R/R_\star$	$0.01596^{+0.00053}_{-0.00053}$	$0.01597^{+0.00055}_{-0.00054}$	$0.01584^{+0.00052}_{-0.00053}$
Kepler-223 c Parameters:			
P (d)	$9.84584^{+0.00085}_{-0.00053}$	$9.84564^{+0.00052}_{-0.00051}$	$9.84613^{+0.00046}_{-0.00045}$
T_0 (BJD-2454900)	$800.1461^{+0.0049}_{-0.0040}$	$800.1459^{+0.0050}_{-0.0039}$	$800.1489^{+0.0061}_{-0.0047}$
$e \cdot \cos(\omega)$	$0.030^{+0.050}_{-0.047}$	$0.029^{+0.041}_{-0.038}$	$-0.010^{+0.019}_{-0.022}$
$e \cdot \sin(\omega)$	$0.134^{+0.027}_{-0.156}$	$0.139^{+0.021}_{-0.050}$	$0.060^{+0.033}_{-0.038}$
$\|i - 90\|$ (°)	$0.0^{+1.4}$	$0.0^{+1.3}$	$0.0^{+1.5}$
Ω (°)	0.0 (fixed)	0.0 (fixed)	0.0 (fixed)
$M/M_\star$	$0.0000157^{+0.0000048}_{-0.0000038}$	$0.0000152^{+0.0000048}_{-0.0000033}$	$0.0000189^{+0.0000032}_{-0.0000033}$
$R/R_\star$	$0.01847^{+0.00055}_{-0.00056}$	$0.01842^{+0.00053}_{-0.00053}$	$0.01833^{+0.00056}_{-0.00057}$
Kepler-223 d Parameters:			
P (d)	$14.78881^{+0.00049}_{-0.00040}$	$14.78869^{+0.00030}_{-0.00027}$	$14.78862^{+0.00025}_{-0.00024}$
T_0 (BJD-2454900)	$804.8502^{+0.0022}_{-0.0023}$	$804.8504^{+0.0023}_{-0.0024}$	$804.8492^{+0.0022}_{-0.0023}$
$e \cdot \cos(\omega)$	$0.020^{+0.031}_{-0.030}$	$0.020^{+0.026}_{-0.024}$	$0.000^{+0.011}_{-0.013}$
$e \cdot \sin(\omega)$	$0.017^{+0.023}_{-0.076}$	$0.010^{+0.020}_{-0.032}$	$-0.001^{+0.015}_{-0.021}$
$\|i - 90\|$ (°)	$2.02^{+0.29}_{-0.52}$	$2.06^{+0.26}_{-0.32}$	$1.68^{+0.30}_{-0.29}$
Ω (°)	0.0 (fixed)	0.0 (fixed)	0.0 (fixed)
$M/M_\star$	$0.0000203^{+0.0000040}_{-0.0000039}$	$0.0000240^{+0.0000039}_{-0.0000035}$	$0.0000225^{+0.0000032}_{-0.0000032}$
$R/R_\star$	$0.02791^{+0.00056}_{-0.00064}$	$0.02800^{+0.00052}_{-0.00059}$	$0.02756^{+0.00053}_{-0.00058}$
Kepler-223 e Parameters:			
P (d)	$19.72553^{+0.00067}_{-0.00071}$	$19.72567^{+0.00055}_{-0.00054}$	$19.72568^{+0.00054}_{-0.00048}$
T_0 (BJD-2454900)	$817.5231^{+0.0055}_{-0.0048}$	$817.5237^{+0.0055}_{-0.0051}$	$817.5231^{+0.0053}_{-0.0046}$
$e \cdot \cos(\omega)$	$0.017^{+0.042}_{-0.033}$	$0.017^{+0.026}_{-0.024}$	$0.013^{+0.014}_{-0.014}$
$e \cdot \sin(\omega)$	$0.045^{+0.032}_{-0.077}$	$0.039^{+0.023}_{-0.032}$	$0.033^{+0.016}_{-0.023}$
$\|i - 90\|$ (°)	$1.95^{+0.25}_{-0.45}$	$2.00^{+0.21}_{-0.27}$	$1.69^{+0.25}_{-0.24}$
Ω (°)	0.0 (fixed)	0.0 (fixed)	0.0 (fixed)
$M/M_\star$	$0.0000102^{+0.0000044}_{-0.0000042}$	$0.0000145^{+0.0000039}_{-0.0000036}$	$0.0000130^{+0.0000031}_{-0.0000029}$
$R/R_\star$	$0.02450^{+0.00076}_{-0.00077}$	$0.02466^{+0.00074}_{-0.00076}$	$0.02421^{+0.00069}_{-0.00068}$

DEMCMC posterior probability median values and 68% confidence intervals for all model parameters at $T_{epoch} = 800.0$ (BJD $- 2,454,900$). Three parameter sets are given with fixed stellar mass: (1) DEMCMC results with eccentricity constraint $\mathcal{C}_1$; (2) the subset of the $\mathcal{C}_1$ DEMCMC results that retain only those solutions that are stable for 10^6 years ($\mathcal{C}_2$); and (3) Laplace-angle constraint $\mathcal{C}_3$ and fixed $\Omega_i = 0$ for $i = $ b, c, d, e.

Extended Data Table 3 | Best-fit Kepler-223 initial conditions

Planet	Period (d)	T_0 (BJD-2454900)	e	i (°)	Ω (°)	ω (°)	Mass (M_{Jup})	Radius ($R_p/R_\star$)
b	7.384720365879194	801.516262774051825	0.105758145660053	90.701847866139545	0.0	62.597372675420416	0.022730704097050	0.015954404145479
c	9.845453934132928	800.146170501596430	0.172729064427036	90.30181103839879	0.0	85.015828120049491	0.017312231285438	0.018346434846992
d	14.788902636701252	804.851045349929109	0.037330052890247	92.189693102657941	0.0	76.465729705828863	0.019623186719198	0.027674878130791
e	19.726218957815664	817.521944355066694	0.051464531998599	92.056638725826986	0.0	111.706814565803512	0.009576406850388	0.024759859857039
Stellar Parameters:	1.125 $M_\star$ ($M_\odot$)			$R_\star$ ($R_\odot$):	1.744528317200141	c_1:	0.479330549583184	c_2: 0.2 _dilute_: 0.11202
b	7.384583733215798	801.513943095097261	0.061453702027857	91.105539095271382	0.0	37.604238003695137	0.020503806935496	0.015793288256059
c	9.845639757204141	800.144691508369419	0.112391047984129	91.085286013475226	0.0	86.059011138583742	0.019192688432573	0.018609959659302
d	14.788880252356291	804.849755312464254	0.026604678672708	91.966288309512123	0.0	58.807213313926120	0.025560722351934	0.028232411829371
e	19.725687523818440	817.519383441790524	0.060783217179960	91.806556478578258	0.0	76.156009027159996	0.015467248730564	0.024265426463497
Stellar Parameters:	1.125 $M_\star$ ($M_\odot$)			$R_\star$ ($R_\odot$):	1.683974231305496	c_1:	0.532243950638929	c_2: 0.2 _dilute_: 0.11202

Best-fit initial planet conditions found by DEMCMC under $\mathcal{C}_1$ (top) and $\mathcal{C}_3$ (bottom) constraints at $T_{epoch} = 800.0$ (BJD $-$ 2,454,900) with $\chi^2 = 746{,}480$ and $\chi^2 = 746{,}489$, respectively. M_{Jup}, mass of Jupiter.